PHYSICAL REVIEW B **91**, 020407(R) (2015)

Strong competition between orbital ordering and itinerancy in a frustrated spinel vanadate

J. Ma,[1] J. H. Lee,[2] S. E. Hahn,[1] Tao Hong,[1] H. B. Cao,[1] A. A. Aczel,[1] Z. L. Dun,[3] M. B. Stone,[1] W. Tian,[1] Y. Qiu,[4,5] J. R. D. Copley,[4] H. D. Zhou,[3] R. S. Fishman,[2,*] and M. Matsuda[1,†]

[1]*Quantum Condensed Matter Division, Oak Ridge National Laboratory, Oak Ridge, Tennessee 37831, USA*
[2]*Materials Science and Technology Division, Oak Ridge National Laboratory, Oak Ridge, Tennessee 37831, USA*
[3]*Department of Physics and Astronomy, University of Tennessee, Knoxville, Tennessee 37996, USA*
[4]*NIST Center for Neutron Research, Gaithersburg, Maryland 20899-6102, USA*
[5]*Department of Materials Science and Engineering, University of Maryland, College Park, Maryland 20742, USA*

(Received 9 June 2014; revised manuscript received 30 December 2014; published 26 January 2015)

The crossover from localized to itinerant electron regimes in the geometrically frustrated spinel system $Mn_{1-x}Co_xV_2O_4$ is explored by neutron-scattering measurements, first-principles calculations, and spin models. At low Co doping, the orbital ordering (OO) of the localized V^{3+} spins suppresses magnetic frustration by triggering a tetragonal distortion. At high Co doping levels, however, electronic itinerancy melts the OO and lessens the structural and magnetic anisotropies, thus increasing the amount of geometric frustration for the V-site pyrochlore lattice. Contrary to the predicted paramagentism induced by chemical pressure, the measured noncollinear spin states in the Co-rich region of the phase diagram provide a unique platform where localized spins and electronic itinerancy compete in a geometrically frustrated spinel.

DOI: 10.1103/PhysRevB.91.020407 PACS number(s): 61.05.fm, 75.10.Jm, 75.25.Dk, 75.30.Et

The competition between localized and itinerant behavior triggers many intriguing phenomena such as metal-insulator transitions [1], colossal magnetoresistance [2], and superconductivity in heavy fermion [3] and Fe-based materials [4]. Likewise, the transformation from itinerant to localized spins in geometrically frustrated systems can create exotic phases by modifying the relationship between the spin, orbital, and lattice [5] degrees of freedom. Although the competing effects of localized and itinerant behavior on magnetic frustration have been rather extensively investigated on triangular and pyrochlore lattices, they have rarely been explored for the frustrated spinel AB_2O_4.

Underlying the rich phase diagrams of spinels are the tunable magnetic interactions between the A and B sites and the geometric frustration experienced by the B sites on a pyrochlore lattice. Spinel vanadates exhibit additional intriguing characteristics due to the orbital ordering (OO) [6–12] of the partially filled ($3d^2$) B sites. Because itinerancy interferes with OO [9–13], it enriches the complex interplay between the magnetic, orbital, and lattice degrees of freedom. But this complexity also makes it difficult to provide a detailed microscopic understanding of this system [8,14–18]. Through substitution of the A site, we systematically study the competition between OO and itinerancy in the spinel vanadates. In particular, the modified spin, orbital, and lattice couplings in $Mn_{1-x}Co_xV_2O_4$ are used to reveal the competing effects of OO and itinerancy on the coupled magnetic and structural phase transitions [13,19,20].

Elastic and inelastic neutron-scattering (INS) measurements are combined with first-principles calculations and spin models to study single crystals of $Mn_{1-x}Co_xV_2O_4$. Because Co^{2+} is the smallest 2+ magnetic cation that can be introduced on the A site, it exerts strong chemical pressure. Previously this chemical pressure was expected to induce itinerancy and consequent paramagnetism [13]. However, we find that the itinerancy driven by Co doping unexpectedly enhances both the para-to-collinear and collinear-to-noncollinear (CL to NC) transition temperatures, T_{CL} and T_{NC}. While the magnetic ground state of the V spins remains a two-in/two-out state throughout the entire doping range, that state has different origins in the itinerant (Co-rich) and localized (Co-poor) regimes.

At low Co doping, OO suppresses frustration by triggering cubic-to-tetragonal structural and CL to NC (two-in/two-out) magnetic transitions at $T_S = T_{NC}$. However, at high Co doping, itinerancy weakens the structural transition ($T_S < T_{NC}$) by melting the OO and revives the suppressed frustration. Despite the complete disappearance of OO and of the structural transition, the novel two-in/two-out is stabilized by the revived frustration and the enhanced Co-V exchange at an even higher temperature than at low doping levels.

Neutron-diffraction experiments were performed at the four-circle diffractometer (HB-3A) and the triple-axis spectrometer (HB-1A) at the High Flux Isotope Reactor (HFIR) of the Oak Ridge National Laboratory (ORNL). The data were refined by the Rietveld method using FULLPROF [21]. INS data were collected utilizing the thermal (HB-1) and cold (CG-4C) triple-axis spectrometers at HFIR, ORNL, with fixed final energies of 14.7 meV at HB-1 and 5 or 3.5 meV at CG-4C, respectively; and the time-of-flight (TOF) spectrometers, DCS, at National Institute of Standards and Technology (NIST) [22] and SEQUOIA, at the Spallation Neutron Source (SNS) with fixed incident energies of 25.25 and 30 meV, respectively. The TOF data were analyzed with DAVE [23]. Error bars in the figures represent one standard deviation.

The Co-doping dependence of the crystal and magnetic structures and OO was determined by single-crystal neutron-diffraction measurements. Figures 1(a) and 1(b) show the

*Authors to whom correspondence should be addressed: fishmanrs@ornl.gov
†Authors to whom correspondence should be addressed: matsudam@ornl.gov

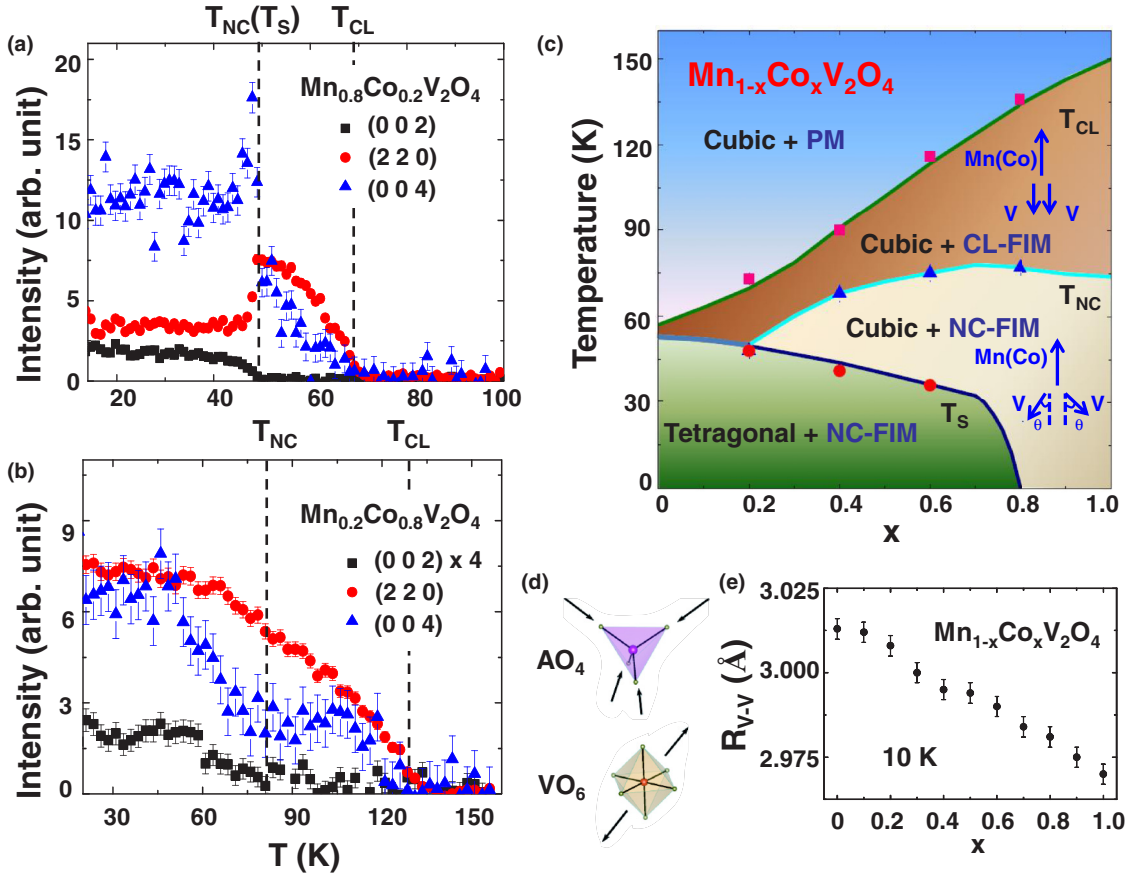

FIG. 1. (Color online) Temperature dependence of the Bragg peaks, (002) (squares), (220) (circles), and (004) (triangles) in (a) $Mn_{0.8}Co_{0.2}V_2O_4$ and (b) $Mn_{0.2}Co_{0.8}V_2O_4$. The background has been subtracted. (c) The temperature versus Co-doping content (x) phase diagram. The para-to-CL magnetic transition temperature T_{CL}, the CL-NC ferrimagnetic phase transition temperature T_{NC}, and the cubic-to-tetragonal lattice transition temperature T_S are determined from the magnetic susceptibility/heat capacity (solid lines) and neutron-scattering experiments (square, triangle, and circle for the transitions). (d) AO_4 ($A = Mn^{2+}/Co^{2+}$) tetrahedron and VO_6 octahedron. (e) The x dependence of the V^{3+}-V^{3+} distance $R_{V\text{-}V}$ at 10 K (black dots).

temperature dependence of the (002), (220), and (004) Bragg peaks for $Mn_{1-x}Co_xV_2O_4$ ($x = 0.2$ and 0.8). A ferrimagnetic (FIM) signal develops below T_{CL} at the symmetry-allowed Bragg positions (220) and (004). While the (002) peak is forbidden by symmetry, the observed scattering intensity below T_{NC} signals the formation of an antiferromagnetic (AFM) spin structure in the ab plane. The onset of the (002) magnetic reflection marks the CL-NC magnetic transition at T_{NC}. The (004) reflection, which also increases in intensity below T_{NC}, provides a measure of both magnetic transitions. For $x = 0.2$, the intensities of the (220) and (004) Bragg peaks rise at ~70 K (T_{CL}) due to the para-to-CL magnetic transition. The intensity of (220) peak drops sharply at ~50 K ($T_S = T_{NC}$) due to the cubic-to-tetragonal structural transition. Hence, T_{NC} coincides with T_S through $x \approx 0.2$ [6]. For $x > 0.2$ the two transitions separate with $T_S < T_{NC}$. At $x = 0.8$ the structural transition disappears, while two magnetic transitions are observed with $T_{CL} \sim 150$ K and $T_{NC} \sim 80$ K. In high Co-doped compounds, x-ray diffraction and heat capacity measurements also suggest the absence of a structural transition [20].

To summarize the results as shown in the phase diagram in Fig. 1(c): we find for (i) $x \leqslant 0.2$: a para-to-CL magnetic transition at T_{CL} and a cubic-to-tetragonal structural transition that coincides with the CL-NC transition at $T_S = T_{NC} < T_{CL}$; (ii) $0.2 < x < 0.8$: the CL-NC and cubic-to-tetragonal transitions are decoupled with $T_S < T_{NC} < T_{CL}$; and (iii) $x \geqslant 0.8$: no structural transition is observed down to 5 K but two magnetic phase transitions appear with $T_{NC} < T_{CL}$. Both T_{CL} and T_{NC} increase while T_S gradually decreases with Co^{2+} doping. The detailed measurements used to map the phase diagram are provided in Supplementary Information (SI) A and B [24].

The microscopic effect of Co doping can be understood by considering the structures of the AO_4 tetrahedra and VO_6 octahedra. In the high-temperature cubic phase ($Fd\bar{3}m$), the interior angles of the AO_4 tetrahedra are $\angle$O-A-O = 109.7°. With Co doping, the A-O bond length decreases from 2.041 ($x = 0$) to 1.984 Å ($x = 0.8$), thereby applying chemical pressure along the A-O direction, Fig. 1(d). Each VO_6 octahedra stretches along the ⟨111⟩ direction, producing the local trigonal distortion shown in Fig. 1(d). Due to this distortion, the 12 O-V-O interior angles in the VO_6 octahedra split away from 90° into two different angles. With Co^{2+} doping, the difference between the two O-V-O angles decreases from 12.3(2)° ($x = 0$) to 10.0(2)° ($x = 0.8$). Simultaneously, the V-O bond length shrinks from 2.023(1) ($x = 0$) to 2.012(1) Å

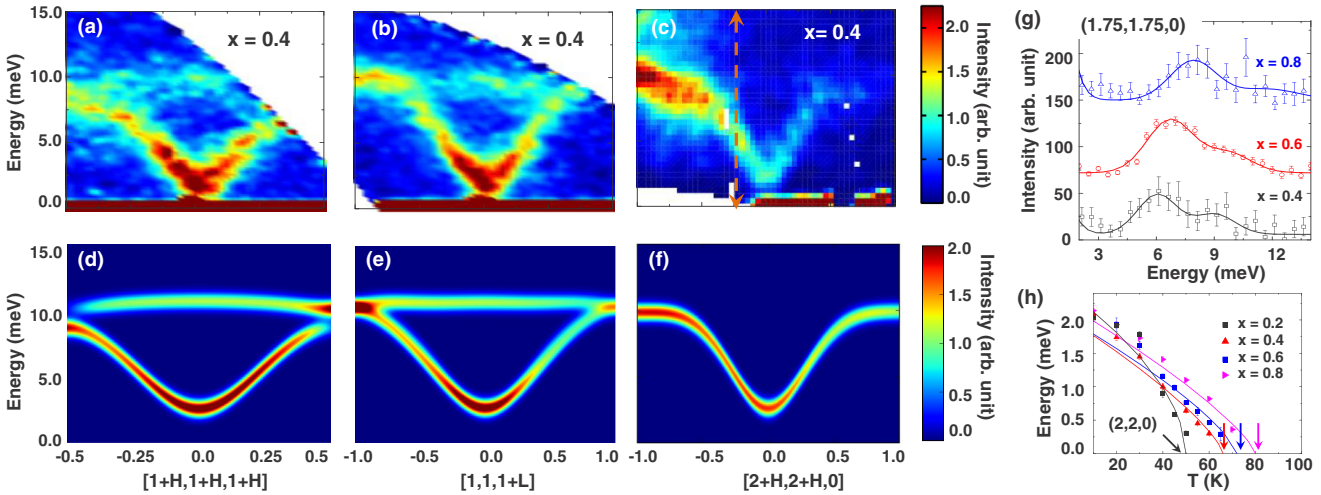

FIG. 2. (Color online) (a)–(c) INS results for the magnetic excitations of $Mn_{0.6}Co_{0.4}V_2O_4$ at 8 K. (d)–(f) The calculated excitation spectra using the Hamiltonian, Eq. (1). The arrow line in (c) represents the position of the constant-Q cut. (g) The constant-Q cuts at (1.75 1.75 0) along [H H 0] direction in $Mn_{1-x}Co_xV_2O_4$ measured at 8 K, $x = 0.4$, 0.6, and 0.8. The curves in (g) are Gaussian fits and guides to the eye. Note that the low-energy spin-wave branch hardens with increase of Co doping. (h) The spin-wave energy gap at the magnetic zone center (2 2 0) in $Mn_{1-x}Co_xV_2O_4$. The curves in (h) are power-law fits.

($x = 0.8$) and the V-V bond length ($R_{\text{V-V}}$) shrinks from 3.013 to 2.975 Å, which increases both chemical pressure and structural isotropy.

The structural phase diagram reflects the evolution of these bond length and angle parameters with Co doping. Although the crystal space group changes from $Fd\bar{3}m$ (cubic) to $I4_1/a$ (tetragonal) with decreasing temperature when $x < 0.8$, it remains $Fd\bar{3}m$ (cubic) down to the lowest temperature studied when $x \geqslant 0.8$. By contrast, most spinel vanadates exhibit structural transitions with decreasing temperature [6–12], so the behavior of the $x \geqslant 0.8$ samples is anomalous.

On the other hand, magnetic structures are tightly coupled to the crystal structure and very sensitive to the Co doping level. Below T_{CL}, the Mn/Co moments are aligned parallel to the c axis. Above T_{NC}, the V^{3+} moments point along the c axis and are antiparallel to the Mn/Co moments. Below T_{NC}, the V^{3+} moments form the two-in/two-out configuration as observed previously in MnV_2O_4 [25] and FeV_2O_4 [26]. The canting of the V^{3+} moments away from the c axis starts below 70 K and reaches 22.1(1.8)° at 10 K for $x = 0.8$, smaller than 35.7(1.5)° and 36.2(1.5)° for $x = 0.0$ and 0.2 at 10 K, respectively. Meanwhile, the V^{3+} ordered moment initially increases from 0.95(4) ($x = 0.0$) to 1.03(7) μ_B ($x = 0.2$), then decreases to 0.61(3) μ_B ($x = 0.8$) at 10 K. The enhancement of the V^{3+} moment from $x = 0.0$ to 0.2 clearly reflects the reduced orbital moment associated with Co doping. Contrary to the prediction that the small Co^{2+} cation triggers paramagnetism [13], we find that the ordered V magnetic moment does not disappear for Co-rich ($x \geqslant 0.8$) compounds and their ordering temperatures (T_{CL}, T_{NC}) even increase with doping, as shown in Fig. 1(c).

To confirm the itinerancy-induced origin of the NC states, the exchange interactions and anisotropies were evaluated from the INS spectra of spin-wave excitations. Since the interaction between the A^{2+} ions is known to be small [27–29], the interactions between the A^{2+} and V^{3+} ions can be estimated from the dispersion of the low-energy acoustic mode. For $x = 0.4$, the measured dispersions along the ⟨110⟩ direction are plotted in Fig. 2(a). Notice that two magnetic modes have been observed, as shown in Fig. 2(c), which is the same as in MnV_2O_4 [29], and the spin-wave velocities increase with Co doping. Measured at the (220) zone center, the spin-wave gap is plotted as a function of temperature and doping in Fig. 2(h). As in MnV_2O_4 [25] and FeV_2O_4 [26], the spin-wave gap below T_{NC} is produced by an easy-axis anisotropy along the cubic diagonal of each V tetrahedron, which also cants the V^{3+} moments away from the c axis. Intriguingly, this spin-wave gap is almost independent of Co doping, Fig. 2(h). Ignoring J^{ab}_{BB} and J^{c}_{BB}, the spin-wave gap would be proportional to $\sqrt{J_{AB} \times D_B}$. We conclude that a roughly constant spin-wave gap of about 2 meV is maintained by the balance between the enhanced J_{AB} and the suppressed D_B associated with the itinerancy of the V^{3+} ions. In particular, the suppressed D_B promotes frustration in the spinel structure [30].

Spin-wave theory was used to understand the microscopic origin of the itinerancy-driven NC states in the absence of OO. These calculations were based on the Hamiltonian with six inequivalent sublattices,

$$\begin{aligned} H = & -J_{AB} \sum_{(p,q)(i,j,k,l)} (\boldsymbol{S}_p + \boldsymbol{S}_q) \cdot (\boldsymbol{S}_i + \boldsymbol{S}_j + \boldsymbol{S}_k + \boldsymbol{S}_l) \\ & - J^{ab}_{BB} \left(\sum_{i,j} \boldsymbol{S}_i \cdot \boldsymbol{S}_j + \sum_{k,l} \boldsymbol{S}_k \cdot \boldsymbol{S}_l \right) \\ & - J^{c}_{BB} \sum_{(i,j)(k,l)} (\boldsymbol{S}_i + \boldsymbol{S}_j) \cdot (\boldsymbol{S}_k + \boldsymbol{S}_l) \\ & + D_A \sum_{r=p,q} (\hat{z} \cdot \boldsymbol{S}_r)^2 + D_B \sum_{s=i,j,k,l} (\hat{u_s} \cdot \boldsymbol{S}_s)^2. \end{aligned} \tag{1}$$

The inequivalent A sites are given by subscripts p and q, and the inequivalent B sites are given by subscripts i, j, k, and l. Isotropic exchange constants (J_{AB}, J^{ab}_{BB}, and J^{c}_{BB}) describe the nearest-neighbor interactions, Fig. 3(c). For the A-site spins,

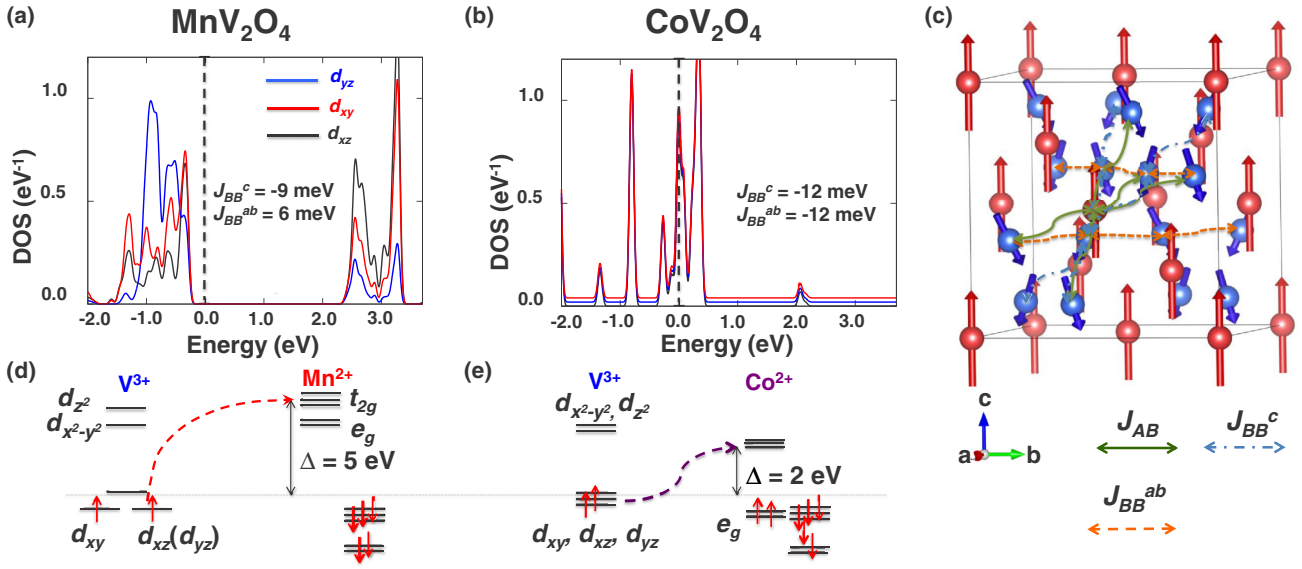

FIG. 3. (Color online) (a) and (b) Density-of-states for AFM MnV_2O_4 and CoV_2O_4, respectively. (c) NC state of $Mn_{1-x}Co_xV_2O_4$. J_{AB}, J_{BB}^{ab}, and J_{BB}^{c} are the exchange interactions between nearest-neighbor sites. (d) and (e) Orbital energies estimated from DFT calculations. $|J_{A\text{-}V}|$ is inversely proportional to the energy gap Δ. Only up-spin energy levels are shown for V^{3+} for simplicity.

the easy-axis anisotropy D_A is along the c axis while for the B-site spins, the easy-axis anisotropy D_B is along the local $\langle 111 \rangle$ direction ($\hat{us}$). A range of values for S_B and J_{BB}^{ab} produces fits of similar quality (SI C.2) [24]. Parameters best describing the experimental data for $Mn_{0.6}Co_{0.4}V_2O_4$ with $S_A = 4.2\mu_B$, $S_B = 1.4\mu_B$, and $J_{BB}^{ab} = -8.0$ meV were $J_{AB} = -1.8$ meV, $J_{BB}^{c} = 1.1$ meV, $D_B = -9.1$ meV, and $D_A = 0.4$ meV.

The simulated dispersions of $Mn_{0.6}Co_{0.4}V_2O_4$ agree well with the measurements, Figs. 2(d)–2(f). With Co doping we fix the B-site (V) moment while lowering the A-site (Mn/Co) moment. As a result, the exchange J_{AB} for $Mn_{0.6}Co_{0.4}V_2O_4$ is stronger than for MnV_2O_4 (SI C.2) [24]. By inducing electronic itinerancy, density-functional theory (DFT) indicates that Co doping also strengthens both the structural ($c \sim a$) and magnetic ($J_{BB}^{ab} \sim J_{BB}^{c}$) isotropies, as shown in Figs. 3(a) and 3(b). If the J_{AB} interactions were not enhanced by Co doping, the remanent magnetic anisotropies along the diagonals of the V tetrahedra would transform the V spin state into an all-in/all-out structure. Due to the enhanced J_{AB}, however, the ground state of the V spins remains the same isosymmetric two-in/two-out state found for small Co doping.

With the orbital energies of both the A and B ions estimated from DFT (SI D) [24], the origin of the enhanced J_{AB} is explained in Figs. 3(d) and 3(e). The large energy difference (∼5 eV) between the occupied V and Mn d states weakens the exchange between Mn and V. By filling the e_g level, Co doping significantly lowers the t_{2g} level and enhances the exchange interaction between Co and V. DFT calculations reveal that the AFM J_{AB} is significantly enhanced in CoV_2O_4 (−2.5 meV) compared to MnV_2O_4 (−1.2 meV). Although the V electrons are delocalized by Co doping, the enhanced J_{AB} causes T_{CL} to grow. Furthermore, the enhanced magnetic exchange isotropy ($J_{BB}^{ab} \sim J_{BB}^{c}$) driven by orbital quenching [Fig. 3(b)] stabilizes the isosymmetric NC phase and raises T_{NC}. Therefore, the induced itinerancy strengthens both the CL and NC phases even without OO.

Induced itinerancy is closely related to $R_{V\text{-}V}$. At 10 K, Fig. 1(e) shows that $R_{V\text{-}V}$ remains almost constant up until $x = 0.2$, then begins to decrease. Based on our DFT calculations, the shorter $R_{V\text{-}V}$ induces itinerant electronic behavior, as shown in Figs. 3(a) and 3(b), thereby suppressing OO. Due to the disappearance of OO by the itineracy, T_S falls with Co doping.

As outlined in Fig. 4, the isosymmetric NC states have distinct origins for low and high x. For low Co doping, the OO of the V ions relieves the magnetic frustration by triggering a tetragonal structure transition ($c/a < 1$) and induces the two-in/two-out spin state. The Mn-V interactions only increase the canting angle while maintaining the two-in/two-out. If only the isotropic V-V interactions and the remanent local V anisotropy

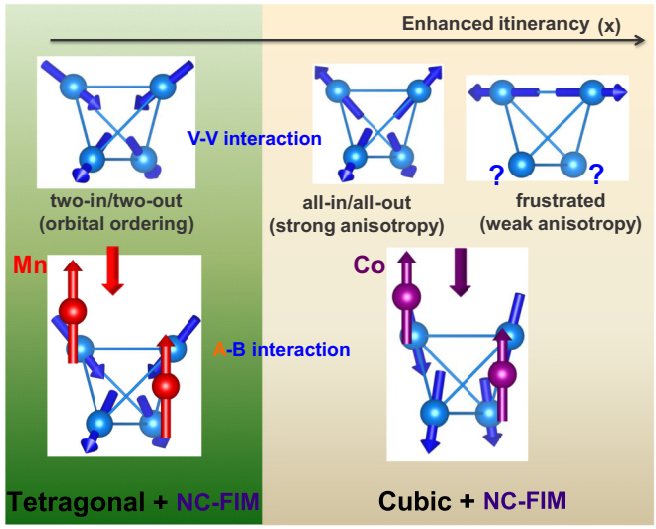

FIG. 4. (Color online) The hierarchical magnetic states with V-V and V-Mn/Co interactions and the distinct origins of isosymmetric phase transition with Co doping (x).

were considered, Co doping would produce an all-in/all-out spin state. However, the strong AFM J_{AB} between the Co and V sites stabilizes the observed two-in/two-out state in the high Co-doping compounds. Perturbations such as pressure may further strengthen the electronic itinerancy, weakening the remanent anisotropy and enhancing the magnetic frustration.

To summarize, $Mn_{1-x}Co_xV_2O_4$ exhibits a rich phase diagram due to the crossover from localized to itinerant electronic regimes. The crystallographic and magnetic structures of compounds with low and high Co doping levels have different physical origins. At low Co doping, OO triggers a cubic-to-tetragonal lattice distortion, accompanied by a CL-to-NC magnetic transition. Co doping contracts $R_{V\text{-}V}$ enhances the electronic itineracy, and revives the magnetic frustration of the pryochlore lattice by weakening the magnetic and structural anisotropies. With further Co doping, OO completely disappears and the magnetic ordering temperatures T_C and T_{NC} are driven higher by the enhanced exchange interaction J_{AB}. Since CoV_2O_4 is located at the crossover between localized and itinerant electron behavior, external pressure may further strengthen itinerancy and magnetic isotropy, enhance geometric frustration, and produce other exotic behavior. The present results provide a microscopic picture for the competition between OO and electronic itinerancy in this frustrated spinel series and suggest a new methodology for studying competing effects with multiple order parameters.

The research at HFIR and SNS, ORNL, were sponsored by the Scientific User Facilities Division (J.M., J.H.L, S.E.H., T.H., H.B.C., A.A.A., M.S., W.T., M.M.) and Materials Science and Engineering Division (J.H.L., R.F.), Office of Basic Energy Sciences, US Department of Energy. S.E.H. acknowledges support by the Laboratory's Director's fund, ORNL. Z.L.D and H.D.Z. thank the support from NSF-DMR through Award DMR-1350002. Work at NIST is supported in part by the National Science Foundation under Agreement No. DMR-0944772. The authors acknowledge valuable discussions with S. Okamoto and G. MacDougall.

[1] M. Imada, A. Fujimori, and Y. Tokura, Rev. Mod. Phys. **70**, 1039 (1998).

[2] A. P. Ramirez, J. Phys.: Condens. Matter **9**, 8171 (1997).

[3] G. R. Stewart, Rev. Mod. Phys. **56**, 755 (1984).

[4] Y. Kamihara, H. Hiramatsu, M. Hirano, R. Kawamura, H. Yanagi, T. Kamiya, and H. Hosono, J. Am. Chem. Soc. **128**, 10012 (2006).

[5] C. Lacroix, P. Mendels, and F. Mila, *Introduction to Frustrated Magnetism: Materials, Experiments, Theory* (Springer, New York, 2001); S. Nakatsuji, Y. Machida, Y. Maeno, T. Tayama, T. Sakakibara, J. van Duijn, L. Balicas, J. N. Millican, R. T. Macaluso, and J. Y. Chan, Phys. Rev. Lett. **96**, 087204 (2006); S. Kumar and J. van den Brink, *ibid.* **105**, 216405 (2010); H. Ishizuka and Y. Motome, *ibid.* **108**, 257205 (2012); M. Udagawa, H. Ishizuka, and Y. Motome, *ibid.* **108**, 066406 (2012); S.-B. Lee, A. Paramekanti, and Y. B. Kim, *ibid.* **111**, 196601 (2013).

[6] V. O. Garlea, R. Jin, D. Mandrus, B. Roessli, Q. Huang, M. Miller, A. J. Schultz, and S. E. Nagler, Phys. Rev. Lett. **100**, 066404 (2008).

[7] G. J. MacDougall, I. Brodsky, A. A. Aczel, V. O. Garlea, G. E. Granroth, A. D. Christianson, T. Hong, H. D. Zhou, and S. E. Nagler, Phys. Rev. B **89**, 224404 (2014).

[8] T. Katsufuji, T. Suzuki, H. Takei, M. Shingu, K. Kato, K. Osaka, M. Takata, H. Sagayama, and T.-H. Arima, J. Phys. Soc. Jpn. **77**, 053708 (2008).

[9] N. Nishiguchi and M. Onoda, J. Phys.: Condens. Matter **14**, L551 (2002).

[10] S. H. Lee, D. Louca, H. Ueda, S. Park, T. J. Sato, M. Isobe, Y. Ueda, S. Rosenkranz, P. Zschack, J. Íñiguez, Y. Qiu, and R. Osborn, Phys. Rev. Lett. **93**, 156407 (2004).

[11] E. M. Wheeler, B. Lake, A. T. M. N. Islam, M. Reehuis, P. Steffens, T. Guidi, and A. H. Hill, Phys. Rev. B **82**, 140406(R) (2010).

[12] A. Kismarahardja, J. S. Brooks, H. D. Zhou, E. S. Choi, K. Matsubayashi, and Y. Uwatoko, Phys. Rev. B **87**, 054432 (2013).

[13] S. Blanco-Canosa, F. Rivadulla, V. Pardo, D. Baldomir, J.-S. Zhou, M. García-Hernández, M. A. López-Quintela, J. Rivas, and J. B. Goodenough, Phys. Rev. Lett. **99**, 187201 (2007).

[14] S. Di Matteo, G. Jackeli, and N. B. Perkins, Phys. Rev. B **72**, 020408(R) (2005).

[15] H. Tsunetsugu and Y. Motome, Phys. Rev. B **68**, 060405(R) (2003).

[16] G.-W. Chern, N. Perkins, and Z. Hao, Phys. Rev. B **81**, 125127 (2010).

[17] S. Sarkar, T. Maitra, R. Valentí, and T. Saha-Dasgupta, Phys. Rev. Lett. **102**, 216405 (2009).

[18] K. Myung-Whun, S. Y. Jang, T. Katsufuji, and A. V. Boris, Phys. Rev. B **85**, 224423 (2012).

[19] A. Kismarahardja, J. S. Brooks, A. Kiswandhi, K. Matsubayashi, R. Yamanaka, Y. Uwatoko, J. Whalen, T. Siegrist, and H. D. Zhou, Phys. Rev. Lett. **106**, 056602 (2011).

[20] A. Kiswandhi, J. S. Brooks, J. Lu, J. Whalen, T. Siegrist, and H. D. Zhou, Phys. Rev. B **84**, 205138 (2011).

[21] J. Rodriguez-Carvajal, Physica B **192**, 55 (1993).

[22] J. R. D. Copley and J. C. Cook, Chem. Phys. **292**, 477 (2003).

[23] R. T. Azuah, L. R. Kneller, Y. Qiu, P. L. W. Tregenna-Piggott, C. M. Brown, J. R. D. Copley, and R. M. Dimeo, J. Res. Natl. Inst. Stan. Technol. **114**, 341 (2009).

[24] See Supplemental Material at http://link.aps.org/supplemental/10.1103/PhysRevB.91.020407 for extra diffractions, raw data at zone center, and details of theoretical calculations.

[25] A. J. Magee, Ph.D. thesis, Royal Holloway, University of London, 2010.

[26] G. J. MacDougall, V. O. Garlea, A. A. Aczel, H. D. Zhou, and S. E. Nagler, Phys. Rev. B **86**, 060414(R) (2012).

[27] R. Nanguneri and S. Y. Savrasov, Phys. Rev. B **86**, 085138 (2012).

[28] T. Suzuki, M. Katsumura, K. Taniguchi, T. Arima, and T. Katsufuji, Phys. Rev. Lett. **98**, 127203 (2007).

[29] J.-H. Chung, J.-H. Kim, S.-H. Lee, T. J. Sato, T. Suzuki, M. Katsumura, and T. Katsufuji, Phys. Rev. B **77**, 054412 (2008).

[30] S. T. Bramwell and M. J. Harris, J. Phys.: Condens. Matter **10**, L215 (1998).